Reversible, stable and uniform SERS in a Y-shaped microfluidic chip: chemical imaging of concentration gradients

Fabien Chauvet

Reversible, Stable and Uniform SERS in a Y-shaped Microfluidic Chip: Chemical Imaging of Concentration Gradients

Submitted version

Accepted version: Microfluidics and Nanofluidics 28, 47 (2024)
https://doi.org/10.1007/s10404-024-02740-0

F. Chauvet

Laboratoire de Génie Chimique, Université de Toulouse, CNRS, Toulouse INP, UTIII, France

Abstract

Imaging of chemical composition in microfluidic chips is addressed using Surface Enhanced Raman Spectroscopy (SERS). The Y-shaped SERS microfluidic chip used is fabricated by xurography and an electrodeposition method is employed to form a thin nanostructured silver layer over the bottom glass wall of the main microchannel. Used as an immobilized SERS substrate, this layer of silver nanocrystals exhibits an analytical enhancement factor of 5.10^4 uniformly distributed over its surface (RSD $< 7\%$). These good performances allow the quantitative imaging of transverse diffusion profiles of Crystal Violet (CV) at low concentrations (10^{-8}-10^{-6} mol/L). The SERS measurement turns out to be reversible at high laser power and this is explained by the thermal desorption of adsorbed CV (photothermal effect). However, too high heating leads to a low amount of adsorbed species and a low SERS signal. This effect is limited by using a fast enough flow inducing a cooling effect. A compromise must be found between laser power and liquid flow rate to enable a reversible and sensitive SERS measurement in the chip. These findings should contribute to the development of imaging, in microfluidic conditions, of the spatiotemporal dynamics of weakly concentrated key molecules involved in chemical, biochemical or biological processes.

keywords: chemical imaging, SERS, co-flow, photothermal effect, adsorption, heat and mass transfers.

*Corresponding author: fabien.chauvet@univ-tlse3.fr; +33 5 61 55 74 68; ORCID 0000-0002-3102-0368

1 Introduction

1.1 Chemical Imaging in microfluidic chips

Microfluidic devices allow precise control of contact, mixing and reaction between given species. In this way, a given chemical or biological system can be studied in situ and subject to stimulant gradients which induce a specific response such as the production and release of given compounds, also in a controlled manner. The spatiotemporal distribution of species can be fully controlled in a microfluidic device.

Consequently, the *imaging* of the chemical composition inside a microfluidic chip is a highly desired feature. This requires a chemical imaging method based on the measurement of light spectra at several positions. The light spectra can be obtained from various spectral measurement methods (luminescence, UV-vis, fluorescence, Raman, IR, ATR-FTIR, etc.) in order to reveal the spatiotemporal variations in chemical composition or simply to allow the imaging of a transparent compound to the naked eye in the microchannel.

The resulting composition map first allows observing in situ the interaction of the system studied with the imposed conditions (fluid injections, microchannel geometry, etc.). The composition map can also be used quantitatively to fit a reaction-transport model, and obtain transport and kinetic parameters from a single experiment. More information is obtained in one shot, from the chemical imaging of the "chemical scene" (gradients), than with conventional techniques based on sampling (and subsequent chemical analyses) of the transient states of the studied system (e.g. as in batch reactor). This further enhances the measurement rate and the high-throughput analysis capability of microfluidic chips.

Chemical imaging in microchannels has been attempted in several works with different methods and purposes. In a first class of studies, single-phase Y-shaped (co-flow) microfluidic chips are used to generate the gradients. The transverse diffusion of solute (without reaction) was measured by fluorescence [1,2] or Raman [3]. Reaction-diffusion dynamics of enzymatic reactions was examined, and kinetic rate constants were extracted, by measuring light emission of a bioluminescent compound [4]. Salmon et al. [5] and Baroud et al. [6] used fluorescence microscopy to extract kinetic parameters of model chemical reactions. Other imaging methods have been employed in Y-shaped microfluidic chips: ATR-FTIR technique to visualize the mixing between the solvents H_2O and D_2O [7], array of optical fibers applied to the detection of pH variations [8], IR imaging to monitor and quantify organometallic chemistry [9] as well as array of electrodes and the associated electrochemical detection applied to the imaging of a focused stream of ferricyanide solution [10]. In other works, droplets generators are used, and the mixing and reaction inside the droplets are observed by Raman [11] or fluorescence [12] measurements. See Zhou et al. [13] for a recent review on optical imaging technologies for microfluidics.

1.2 Surface Enhanced Raman Spectroscopy (SERS) as a chemical imaging method in microfluidic chips

Among the imaging methods previously used (luminescence, fluorescence, IR, Raman and ATR-FTIR spectroscopies, electrochemistry and optical fibers), none combine the three target qualities simultaneously: sensitivity, spatial resolution and "chemical" resolution (wide range of addressable species). Raman spectroscopy appears better than the others for several reasons:

- the Raman signal is intrinsic to each molecule (Raman fingerprint), with narrow bandwidth, enabling specific measurements and multiplexing (simultaneous detection of several species); labelling using Raman probes or tags is also possible
- high spatial resolution, up to $1\ \mu$m with confocal microscopes
- well adapted to measurements in aqueous solutions (contrary to IR) and thus to the study of biological and biochemical systems.

However, Raman spectroscopy suffers from a very low sensitivity (limit of detection $\sim 10^{-3}$ mol/L even for molecules with a high cross-section), that prevents its direct use in applications where the molecules of interest are at low concentration (this is generally the case in biological applications).

The sensitivity can be greatly improved using metallic nanostructures (Ag, Au). The principle is to exploit the phenomenon of plasmon resonance, which induces a significant enhancement of the Raman scattering in the vicinity of the surface of metal nanostructures (over a very short length < 1 nm in the fluid phase) up to a factor of 10^{10} [14]; this results in the so-called Surface Enhanced Raman Spectroscopy (SERS). Raman enhancement requires the presence of hot spots: assembly of nanoparticles (nP) with small distance gap between them, typically when they form aggregates, and/or edge effects with anisotropic or dendritic nanostructures [14].

Raman enhancement requires a close contact between the probed molecules and the metallic surface, thus SERS detection is accompanied with the adsorption of the molecules on the surface of the SERS substrate. By analogy with the relationship between the normal Raman signal intensity I_{Raman} and the concentration of probed molecules c, $I_{Raman} = A_{Raman}(w).c.P.IT$ [15] where $A_{Raman}(w)$ is a function of the Raman shift w describing the shape of the Raman spectrum, P the laser power and IT the integration time, the intensity of the SERS signal intensity I_{SERS} is given by [16]:

$$I_{SERS} = A_{SERS}(w).c_{ads}.P.IT, \tag{1}$$

where $A_{SERS}(w)$ is a function describing the shape of the SERS spectrum and c_{ads} the surface concentration of adsorbed probed molecules. As a consequence, the variation

of I_{SERS} is directly related to the variation of c_{ads}, as experimentally shown by Barbillon et al. [16]. The surface concentration c_{ads} depends on the concentration c of the solution in direct contact with the surface of the SERS substrate. For dilute solutions, the adsorption isotherm is linear and thus c_{ads} is proportional to c. Consequently, spatiotemporal variations of c, at the surface of the SERS substrate, should be obtained by the measurement of I_{SERS}.

The use of SERS in microfluidic chips appears as a win-win combination and this has already led to applications mainly for detection and identification purposes with microfluidic chips [17] in which the composition is spatially uniform. However, the imaging by SERS of spatiotemporal variations in composition, in a microfluidic chip, has not yet been achieved. This is due to some specificities of SERS, related to signal stability, spatial uniformity, reversibility and re-use, which are explained in the sections below.

1.3 Fabrication and integration of immobilized SERS substrates

Immobilized SERS substrate are generally formed by deposition methods before the chip assembly/bonding. The widely used method consists in the synthesis of the metal nP in solution (such as the colloidal synthesis) by controlling both size and shape. Next, the obtained dispersion must be purified (removing by-products and remaining reactants) by separation techniques (dialysis, centrifugal processes, etc.). Then the nP can be deposited on the surface (evaporation, dip coating, etc.) by taking care to control 1) the final assembly in order to favor the formation of hot spots and 2) the adhesion of the nP [18]. This method requires several fabrication steps that could induce a lack of reproducibility and non-uniform substrates. Note that other deposition methods have been attempted such as lithography techniques [18], vapour deposition [19] and pulsed laser photoreduction [20].

1.4 Regeneration of SERS substrates

This adsorption of the probed molecules is sufficiently strong to prevent the removal of the molecules from the metallic surface by simple water flushes [14, 21, 22]. This adsorption, by inducing what is sometimes called the “memory effect”, thus renders the SERS substrate not re-usable. Moreover, this also prevents the return to a base state or the observation of a non-monotonic temporal variation.

In microfluidic devices, SERS substrates have been used either in the form of colloidal nP, dispersed in the flowing solution, or in the form of nanostructures immobilized on a microchannel wall [23]. With dispersed colloidal SERS substrate, flowing in a microchannel, the SERS active surface is continuously renewed that allows the re-use of the system. On the other hand, the degree of aggregation of the nP (which determines

the number of hot spots) must be controlled by adding a given amount of salt in the solution, in order to screen electrostatic repulsions [24]. Therefore, the ionic strength of the solution has to be precisely controlled with dispersed colloidal SERS substrate. Note that increasing the ionic strength could lead to clogging of the microchannels by nP aggregates. This differs from immobilized SERS substrates which have the advantage of not being sensitive to ionic strength that avoids controlling this property and possibly interfering with the system studied. Furthermore, due to their denser structure, they contain more hot spots that induces better enhancements. However, as already mentioned above, immobilized SERS substrates need a specific regeneration process of the surface between each measurement [14, 21, 22]. Various methods have been attempted to regenerate the SERS surface: ultrasonification, heat treatment, solvents [25], wet chemical treatment with $NaBH_4$, self-cleaning photocatalytic SERS substrates, degradation by UV [22], laser-activated deprotection [26], surface replacement from chemical etching followed by metal re-deposition [21] and electrically assisted regeneration [27]. A majority of these methods require modifying the chemical composition inside the microchannel that must be followed by subsequent flushing purification cycles and the other methods require external physical means.

1.5 Performance evaluation of immobilized SERS substrates

The performance of immobilized SERS substrates is first evaluated by the enhancement factor. There are several definitions of this factor [28] and some of them should be considered with caution because of the use of approximations, notably to estimate the number of probed molecules with normal Raman but also, and mostly, the number of probed molecules with SERS. The Analytical Enhancement Factor (AEF), defined by Eq. 2, is as an appropriate functional descriptor, even if it is not an intrinsic property of the substrate [28]:

$$\mathrm{AEF} = \frac{I_{SERS}/c_{SERS}}{I_{Raman}/c_{Raman}}, \tag{2}$$

where I_x is the intensity of either the SERS signal ($x = SERS$) or the normal Raman signal ($x = Raman$) and c_x is the concentration of the compound probed when using either SERS ($x = SERS$) or normal Raman spectroscopy ($x = Raman$). Note that dyes, such as Crystal Violet (CV), are usually used as test molecules to evaluate AEF because they exhibit a high cross-section for Raman signal and thus they enable easy measurements.

The evaluation of the spatial uniformity of the SERS signal is also very important (especially for chemical imaging purpose) although not systematically measured and provided. This latter has been evaluated either by the Relative Standard Deviation (RSD) or by the Relative Amplitude Variation (RAV = (max-min)/2/mean) of the spatial variation of the SERS signal. According to the available reported data, for SERS substrates integrated or not in microchannels, the RSD and RAV of the SERS signal are in

the ranges [$\sim$2, 20%] and [5, 20%] respectively, see Table 1. In the SERS microfluidic chips developed so far, the size of the SERS substrate varies from few micrometers [20] to the typical lateral dimensions of microchannels, i.e. $\sim$1 mm x $\sim$2 cm [29, 30]. The corresponding RSD and RAV are in the ranges [$\sim$2, 7%] and [8, 18%] respectively, Table 1.

Spatial variation of SERS signal	Size of the analyzed surface	SERS substrate integrated in a microfluidic chip ?	Ref
5% (RAV)	0.8x2 cm^2	No	[31]
10-20% (RSD)	-	-	[18]
4% (RSD)	2x3 cm^2	No	[32]
6% (RSD)	not provided	No	[33]
3.4% (RSD)	disk ϕ = 10 cm	No	[34]
3% (RSD)	5x5 μm^2	Yes	[20]
18% (RAV)	10 x 100 μm^2	Yes	[19]
8% (RAV)	1x133 μm^2	Yes	[35]
6.4% (RSD)	2 mm x 100 μm	Yes	[25]
2.32% (RSD)	disk ϕ = 1.5 mm	Yes	[36]
7% (RSD)	1 mm x 4 cm (x12)	Yes	[29]
8% (RAV)	2 mm x 2 cm	Yes	[30]

Table 1: Spatial variations of SERS signal from various works, RAV : Relative Amplitude Variation, RSD : Relative Standard Deviation.

1.6 Stability of the SERS signal

Stability of the SERS signal is also a desired feature. Indeed, the SERS signal can be altered and decreased when using the laser at excessive power (that can be tempting to increase the intensity in case of low AEF). This can lead to modifications of both intensity and shape of the SERS spectra. These modifications may be due to photodegradation (photobleaching) of the probed molecules [37]; in a particular case, the laser light can itself induce the photodegradation of probed molecules during a SERS measurement [38].

Also, under laser illumination, the light absorbed by the nanostructure of the SERS substrate is released as heat and this induces a photothermal effect. The local temperature can reach a hundred degrees that can lead to production of bubbles [39, 40], natural

convection and thermodiffusion [41], the desorption of probed molecules [42], and the degradation of the SERS substrate (thermally enhanced mobility and diffusion of metal nP [43]). The temperature rise depends on the particular configuration (materials and modes of heat transfer: conduction or convection). However, the local temperature rise is generally not measured in SERS studies although it can influence the SERS signal.

1.7 The SERS microfluidic chip and the regeneration method proposed in this work

Here, a new method for the integration of the SERS substrate is presented and evaluated. The method is based on the formation of a silver nanostructure, directly inside a microfluidic chip, by electrodeposition of metallic cations Ag^{+}. More precisely, a specific electrochemical growth regime, obtained without the use of supporting electrolyte, is used. Under such conditions, and also in such confined channel geometry with solution at rest (microchannels generally have a slit shape similar to Hele-Shaw cells in which the used electrochemical growth regime was initially performed [44]), the electrolysis of the dissolved metallic (silver) salt, leads to the fast growth of multi-scale metallic structures commonly called *dendrites*. The latter can either be non-adherent, the structure takes the form of ramified branches which could be fractal or dendritic, or adherent to the bottom wall of the cell, the structure is then much more stable and grows under the form of a thin layer (film) [44, 45]. In the latter case, the bottom wall of the cell must first be covered by a thin non-conducting gold layer serving as adhesion layer [45, 46]. In all cases, the electrodeposition of the metallic phase is driven by a renucleation growth mode of small metal crystals which the size could be around or less than 100 nm depending on the operating parameters (mainly the electrolysis current and the electrolyte/salt concentration) [46].

An adherent thin layer of nanostructured silver is directly integrated in a Y-shaped microfluidic chip from this electrodeposition-based method. This thin layer is formed over the bottom wall of the main microchannel of the chip, as shown in Fig. 1a-c. The performance of the elaborated SERS microfluidic chip is evaluated and discussed in terms of signal stability, analytical enhancement factor, spatial uniformity, reversibility and ability to image concentration gradients (transverse diffusion gradients) of CV.

The stability and reversibility of the SERS signal are specifically addressed by studying the variations of the SERS signal (in terms of both intensity and shape of the spectra). The study is carried out, by varying both the liquid flow rate Q and the laser power P, and by estimating the temperature rise from micro-thermocouple measurements coupled with a 3D simulation of heat transfer.

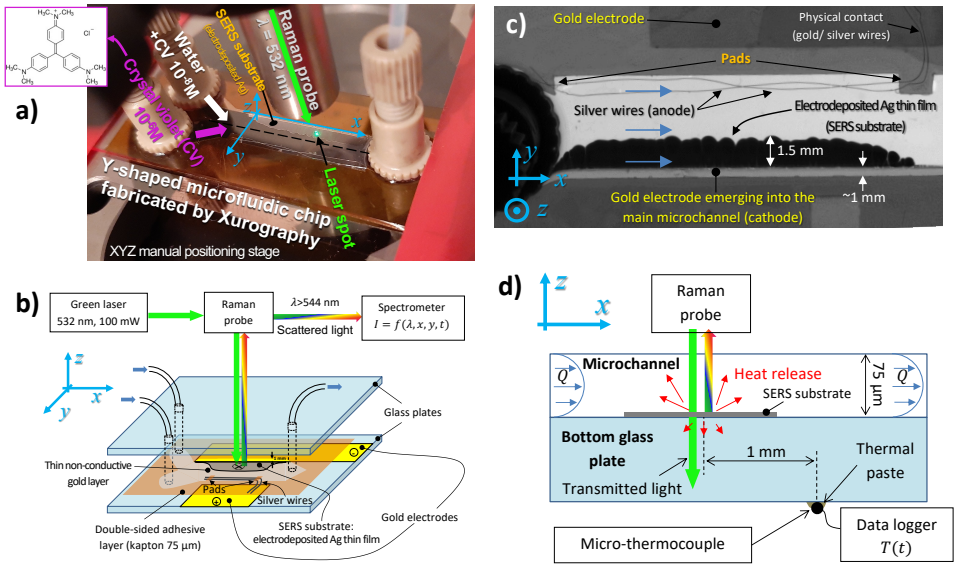

Figure 1: a) A picture of the Y-shaped SERS microfluidic chip in operation, b) schematic exploded view of the chip, c) optical image by transmission (from above) of the main microchannel integrating the electrodeposited silver layer appearing in black (note that this layer is very thin, <200 nm, and does not disturb the flow), the flow direction is indicated by the blue arrows, d) sketch of the chip showing the location of the micro-thermocouple used to estimate laser-induced heating.

2 Experimental set-up and methods

2.1 Elaboration of the SERS microfluidic chip

The microfluidic chip is elaborated by the fast prototyping method called xurography [47–49]. The microchannels of the Y-shaped chip are formed by the digital cut of a double-sided kapton tape (Polydecoupe, France) by a cutting machine (Silhouette Portrait 2), Fig. 1a and b and also Fig. 2 (step 1) in which the fabrication steps are sketched. The width of the main microchannel W is 6 mm, Fig. 2 (step 1).

In the final step, the resulting kapton tape is bonded between two glass plates. The depth of the microchannels h_l is then set by the total thickness of the kapton tape which is $\sim$75 μm (25 μm thick for the kapton film and $\sim$2$\times$25 μm for the adhesive layers), Fig. 2 (step 1). The upper glass plate (1 mm thick) has been drilled beforehand to enable fluid connections (use of nanoports from Idex HS and PTFE tubing). The lower glass

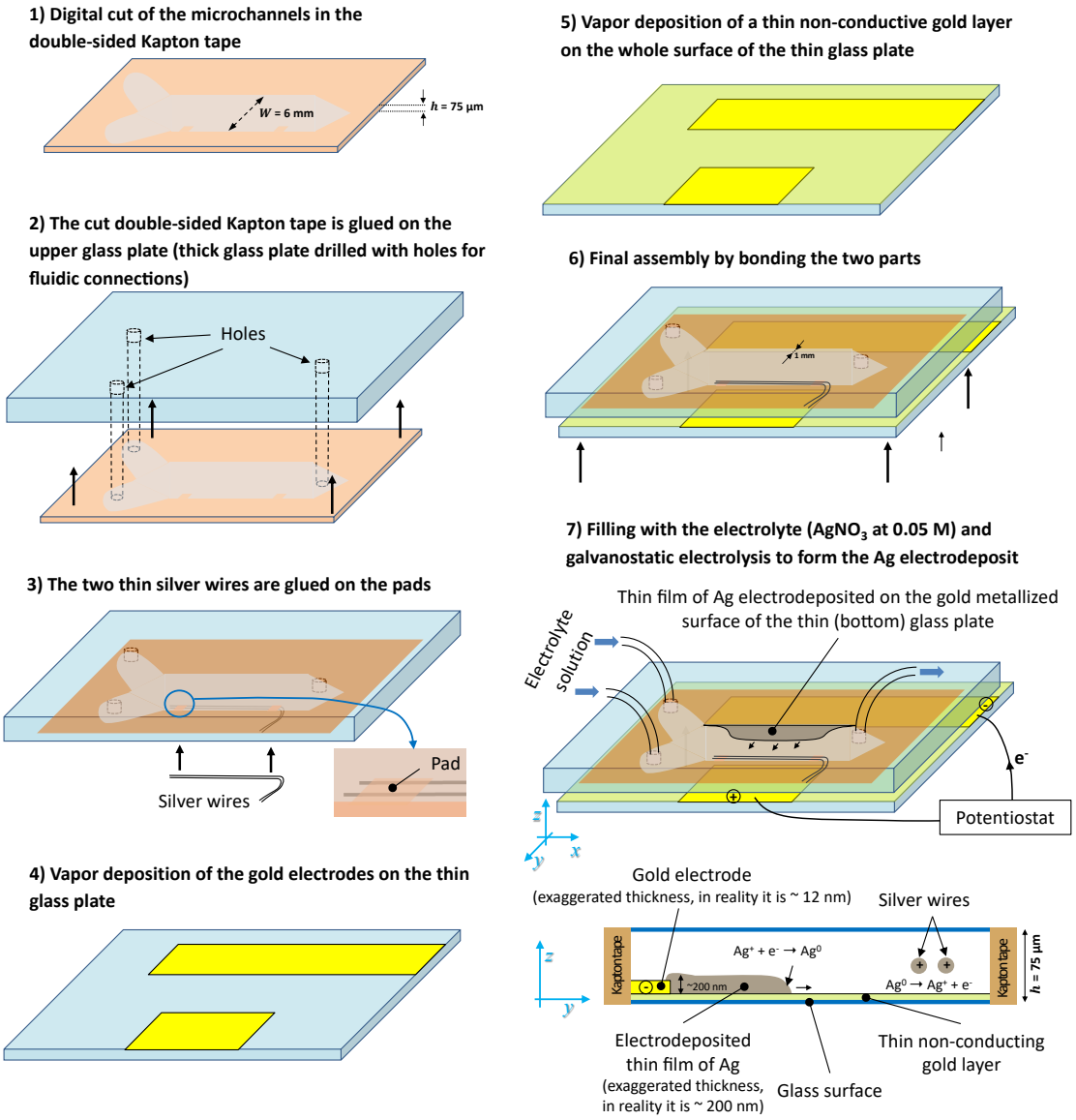

Figure 2: The fabrication steps of the SERS microfluidic chip

plate is a thin cover glass which the thickness is 0.15 mm (VWR).

The cut double-sided kapton tape is first glued on the non-metallized glass plate (the upper glass plate, Fig. 1b), step 2 in Fig. 2. As a sacrificial anode, two thin silver wires (diameter 25 μm) are positioned along the long side of the main microchannel by being glued on two small pads of tape, step 3 in Fig. 2 (see also Fig. 1a-c). Two Ag wires have to be used to avoid electric disconnection because of electrodissolution of silver. The excess lengths of the wires are curved in such a way that they come in physical contact

with the gold electrode deposited on the bottom glass plate (drawn in yellow in Fig. 1b) when the system is bonded (see Fig. 1a) .

To enhance the uniformity and the reproducibility of the surface state, the thin glass plate is subject to a Piranha cleaning (50% H_2SO_4, 50% H_2O_2 at 35%) followed by neutralization in a water bath. Just after this chemical treatment, two gold electrodes, used to perform the electrodeposition inside the main microchannel, are deposited by sputtering trough a simple plastic mask (K550X Sputter Coater, deposit thickness $\sim$12 nm, duration = 2 min), step 4 in Fig. 2. A second gold deposition is carried out on the whole surface but during a shorter time (20 s, deposit thickness $\sim$2 nm) to form the thin non-conductive gold layer (adhesion layer for the silver electrodeposit) between the two thicker gold electrodes, as initially done in previous works [45, 46], step 5 in Fig. 2.

The thin glass plate is aligned, and bonded to the other glass plate, in such a way that the gold cathode slightly exceeds ($\sim$1 mm) into the main microchannel, step 6 in Fig. 2 (see also Fig. 1b-c). A pressure is apply by hand on the whole system to ensure the bonding and also the embedding of the silver wires into the adhesive; their thicknesses are the same (25 μm) and therefore the cell gap is not affected by the presence of the wires. The final depth of the microchannel h_l is determined by thickness measurements using a micrometer (total thickness - thicknesses of glass plates), Fig. 2 (step 6).

After the bonding, the system is filled with the electrolyte $AgNO_3$ at 0.05 M. Keeping the solution stagnant and the cell horizontal, an electric current of 0.5 mA is applied between the two gold electrodes, step 7 in Fig. 2.

At the cathode (the gold electrode, on which a negative polarization is applied, is indicated in step 7 in Fig. 2), the silver ions Ag^+ are reduced to metal silver Ag^0 while at the anode the silver wires are oxidized to Ag^+. The use of a sacrificial anode allows to keep a constant quantity of $AgNO_3$ and also avoid the production of other species which could alter the deposit growth and structure. The constant current electrolysis is typically applied during 100 s. At the cathode, the growth front begins to move rapidly and the final deposit length is typically $\sim$1.5 mm. As already obtained in previous works [45, 46], the deposit grows under the form of a silver layer (thin film) adhering to the thin non-conductive gold layer covering the bottom wall of the main microchannel (see the sketch at the bottom in step 7 in Fig. 2). The thin non-conductive gold layer serves as an adhesion layer for the electrodeposited silver layer [45]. The morphology of the electrodeposited silver layer is a very dense branching pattern with an almost flat growth front, as it can be seen in Fig. 1a and in Fig. 1c where the main microchannel is observed from above by transmission. In this latter Figure, the electrodeposited silver layer appears as black. As it will be discussed below, note at the outset that this silver film is very thin ($<$ 200 nm) and thus does not disturb the Poiseuille flow in the main microchannel (shown with blue arrows in Fig. 1c).

The cathode is set longer than the anode (step 7 in Fig. 2 and Fig. 1a-c) and the resulting current distribution allows avoiding edge effects (at the cathode) which could

induce non-uniform structures. Note that the location and width of the electrodeposited layer can thus be controlled and adjusted inside the microchannel.

After the electrolysis, the cell is flushed by applying a flow of ultrapure water and the chip is ready to be used for SERS measurements.

In Fig. 3, SEM observations (after dismantling the chip in an acetone bath) reveal that the electrodeposited SERS substrate consists of a carpet of cubic silver nanocrystals, Fig. 3a-b (view from above perpendicular to the surface). The individual size of these nanocrystals is around 100 nm and they are uniformly distributed over almost all the deposit length (1.5 mm). This is only near the top of the deposit that the quality of the deposit decreases with larger and less sharp structures. In Fig . 3a, finger-shaped and rounded deposit structures, separated by thin dark zones, are visible. As shown by the magnified views in Fig . 3c, the dark zones correspond to places where the nanostructure is different with the presence of cubic silver nanocrystals of various sizes. These zones correspond to the boundaries of the main growing structures, i.e. the finger-shaped and rounded deposit structures. These structures grow at the same time and by progressively filling the gap between them. This is a specific growth mode for which the diffusion length (for the transport by diffusion of Ag^+ ions) is assumed to be lower than the crystal sizes, that prevents the development of front instability (see Fleury et al. [45] for more details). The thickness of the silver layer is very low $\sim$100 nm as shown by the tilted SEM observations of a cross-section of the silver layer in Fig. 3d (the maximum thickness is lower than 200 nm). Consequently, the silver layer (as well as the two gold deposits) are not expected to disturb the flow in the microfluidic chip. Note that both growth velocity and nanostructure (SEM observations) of the electrodeposited SERS substrate are reproducible.

2.2 Instrumentation

A Raman coupled fiber probe (RPB532, Ocean Optics) is used to illuminate the electrodeposited SERS substrate with a green laser beam (532 nm, 100 mW, Oxxius) and collect the Stokes scattered light (λ >532 nm) which is sent to a spectrometer (HR4000, Ocean Optics) to obtain the SERS spectra, Fig. 1b. The size of the laser spot was determined by illuminating a CCD sensor with the laser beam. The image of the laser spot was processing by fitting a two-dimensional Gaussian function. A standard deviation of 47.94 μm was determined which corresponds to a laser spot, in terms of $1/e^2$ (width at 13.5% of the maximum), of 191.81 μm (FHWM = 112.90 μm). The power of the laser beam is controlled using a variable optical attenuator and a laser power meter (Spectra Physics 407A). The maximum laser power used in this work is 55 mW and the corresponding power density is thus 0.190 kW/cm^2. Concerning light collection of the Raman probe, the depth of field is 2.2 mm (focal length = 7.5 mm and numerical aperture = 0.27). SERS and Raman Spectra are acquired over time during laser illumination and at several locations inside the main microchannel using a manual micrometric XYZ

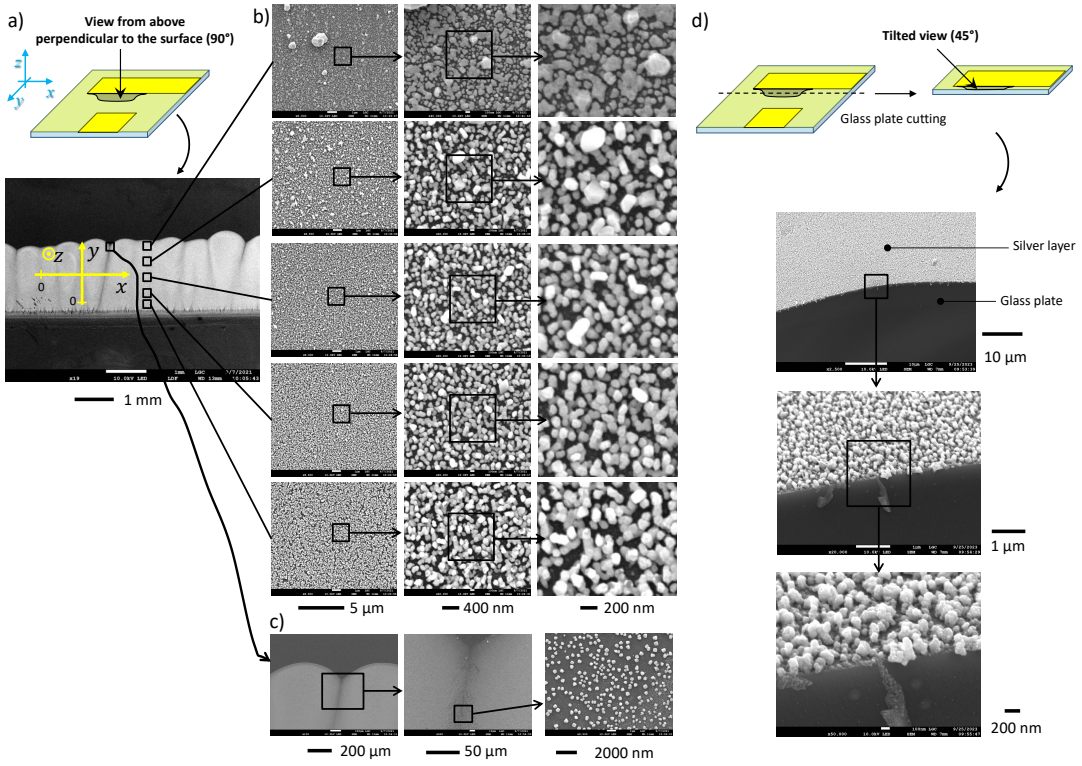

Figure 3: SEM observation of the electrodeposited silver layer.

translation stage.

The heating, induced by the laser, is evaluated by a micro-thermocouple (type K, 150 μm, Radio Spare) placed on the lower surface of the thin bottom glass plate and 1 mm behind the laser spot, downstream of the flow, as sketched in Fig. 1d (the position of the laser spot is not changed during temperature measurements); a thermal paste is used to avoid contact resistance. The temperature signal is recorded by a data-logger (Keysight, DAQ970A).

The liquid flow is applied using using syringe pumps (Harvard Apparatus PHD Ultra). The optical visualizations are performed by transmission using a LED panel, placed below the chip, and a camera PCO pixelfly, associated with a 105 mm macro lens, facing the top glass wall of the chip. The electrolyses are carried out with a potentiostat Autolab PGSTAT100N. The structure of the silver layer is observed by SEM with a Jeol JSM 7100F.

2.3 Chemicals

The electrolytic solution ($AgNO_3$ 0.5 M) is prepared by dissolving $AgNO_3$ (Acros Organics, 99%) in deionized water (18.2 MΩ.cm), no supporting electrolyte is used. Raman and SERS measurements are performed with CV solutions prepared by dissolving crystal violet powder (Fluka) in ultrapure water. Experiments are performed at room temperature (18 - 22 °C).

3 Results & discussion

3.1 Chip operating with uniform concentration of CV inside the main microchannel (no concentration gradients)

3.1.1 Temporal variations of the SERS signal and temperature

A 10^{-6} M solution of CV is continuously injected from one inlet of the SERS microfluidic chip (the other inlet being closed) at a constant flow rate Q in the range from 2 to 1000 μL/min. The concentration in CV is therefore 10^{-6} M throughout the microchannel (no gradients). Next, the green laser is focused on the SERS substrate, at a given x, y location, through both the liquid and the upper glass plate of the chip (Fig. 1a,b,d). The laser illumination is continuous during 1 min with a constant power P in the range from 4 to 55 mW. During the laser illumination, the SERS signal and the temperature measured by the micro-thermocouple $T_{1\,\mathrm{mm}}$ are acquired over time. The acquired SERS spectra of CV, after baseline subtraction, are shown in Fig. 4a-d for extreme values of both Q and P. The temperature rise, $\Delta T_{1\,\mathrm{mm}} = T_{1\,\mathrm{mm}} - T_a$ (where T_a is the ambient temperature), is plotted as a function of time in Fig. 4e-g for various laser powers (10, 25 and 50 mW) and flow rates (from 5 to 1000 μL/min).

Laser-induced temperature rise

In Fig. 4e-g, $\Delta T_{1\,\mathrm{mm}}$ is found to increase during laser illumination. As expected, the higher the laser power P, the higher the temperature rise and the higher the flow rate Q, the less the temperature rise (cooling effect); the temperature rise $\Delta T_{1\,\mathrm{mm}}$ could reach 5°C for $P = 50$ mW and $Q = 5$ μL/min. The temporal variation of the temperature rise $\Delta T_{1\,\mathrm{mm}}$ follows an exponential-like behavior with a rate constant that depends on the flow rate Q and not on laser power P: $\sim$0.10, $\sim$0.30 and $\sim$1.00 s^{-1} for 5, 100, 250 μL/min respectively, for 500 and 1000 μL/min the rate constant is > 2 s^{-1} (beyond the temporal resolution). This thermal dynamics shows that the heat transfer and release is mainly controlled by thermal convection in the liquid flow. The more the flow is fast, the thinner is the thermal boundary layer, above the heated SERS substrate, and the faster is the transient regime before reaching the thermal steady state.

From these measurements, the steady state temperature increase at the laser spot $\Delta T_{ls}^{SS} = T_{ls}^{SS} - T_a$ (where T_{ls}^{SS} is the steady state temperature at the center of the laser spot) is deduced from a 3D numerical simulation of heat transfer in the SERS microfluidic chip, see section 1 of Supplementary Material (SM) for more details about the numerical simulation. Briefly, the principle is to determine the part of laser power absorbed by the Ag nanostructure and released as heat in both the liquid and the glass plates. From the thus deduced absorption coefficient (46%), ΔT_{ls}^{SS} is determined by running the simulation for the investigated values of P and Q. ΔT_{ls}^{SS} is plotted as function of the laser power P for several flow rates Q in Fig. 5. As expected ΔT_{ls}^{SS} increases (linearly) with P and decreases with Q. ΔT_{ls}^{SS} can reach almost 50°C for P = 50 mW and Q = 2 μL/min.

Temporal variations of SERS spectra

Concerning the temporal evolution of the acquired SERS spectra, in Fig. 4a-d, it can be seen that the intensity of SERS signal decreases, just after the onset of laser illumination and for all the values of P and Q investigated; note that the first and last spectra are colored in blue and red respectively. As indicated by the insets (on the right) of each Fig. 4a-d, showing the temporal evolution of the peak amplitude at 1180 cm^{-1} scaled by its maximum initial value, the intensity of SERS signal stabilizes in less than 60 s. The insets (on the left) of each Fig. 4a-d correspond to the SERS spectra scaled by the peak amplitude at 1180 cm^{-1}. These latter superimposed graphs allow to determine if the shape of the spectra changes during laser illumination. To facilitate the analysis of these data, the value of ΔT_{ls}^{SS} is indicated in purple in each inset (on the left) of Fig. 4a-d.

For P = 4 mW and Q = 1000 μL/min (inset, on the left, of Fig. 4c), ΔT_{ls}^{SS} is low (1.7°C) and the shape of the SERS spectra changes very little during laser illumination. The only variation is observed for the usual double peak of CV at 1590 and 1620 cm^{-1}. These peaks correspond to specific vibration modes of benzene rings: non-totally symmetric benzene mode at 1590 cm^{-1} and totally symmetric benzene mode et 1620 cm^{-1} (see [50] for more details). The superposition of the SERS spectra shows that the peak at 1590 cm^{-1} decreases less rapidly than the one at 1620 cm^{-1}. This inversion of intensity for this double peak is also observed for the other cases (Fig. 4a, b, d) but with an inversion intensity that increases with ΔT_{ls}^{SS}. For the extreme case, P = 50 mW and Q = 2 μL/min ($\Delta T_{ls}^{SS} \approx$50°C), Fig. 4b, both peaks are still present but the peak at 1590 cm^{-1} dominates the one at 1620 cm^{-1}.

Since the Raman enhancement of non-totally symmetric modes is known to depend on a charge transfer (chemical) process, and that this is not the case for the Raman enhancement of totally symmetric modes [51], an increase in temperature should favor the enhancement of the peak at 1590 cm^{-1} at the expense of the enhancement of the peak at 1620 cm^{-1}, what is in agreement with what is observed. As a consequence,

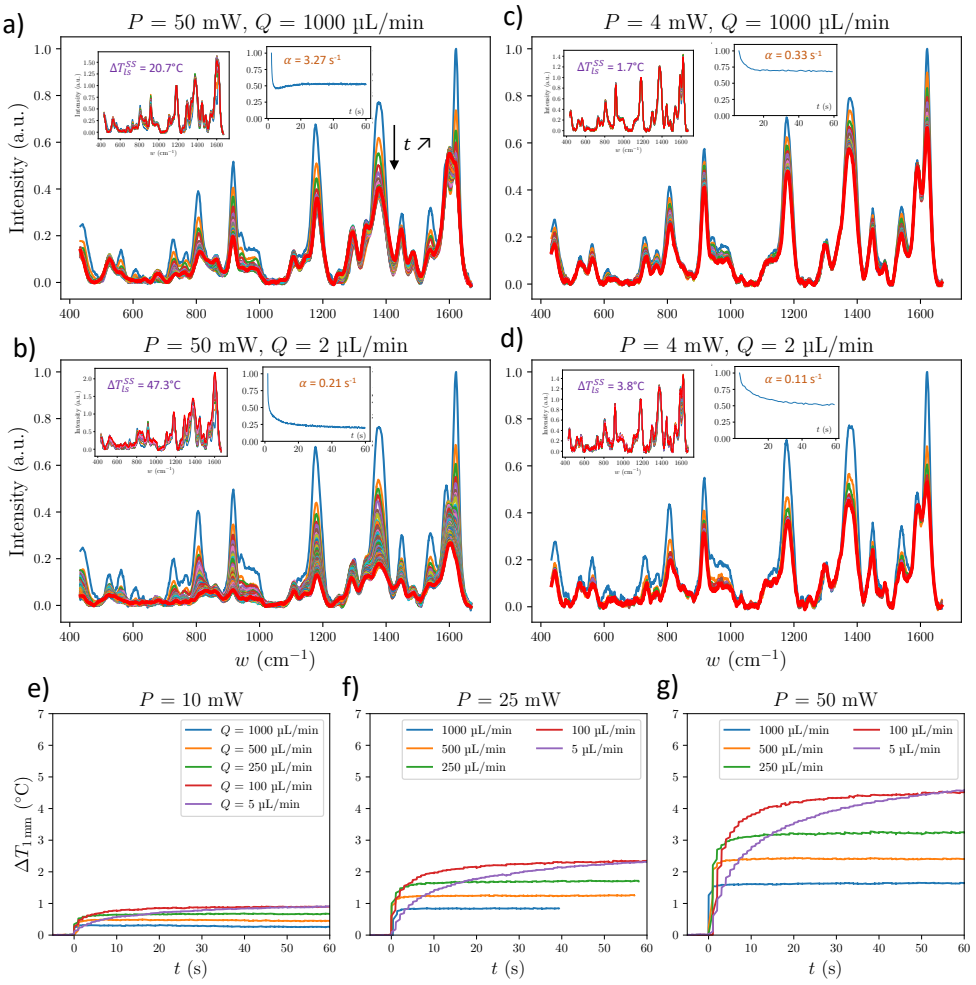

Figure 4: a-d) SERS spectra of Crystal Violet (after baseline subtraction) acquired during laser illumination, the first and the last spectra (after 60 s of illumination) are shown with a blue and a red line respectively. The time interval between each spectra is 0.2 s (IT = 0.1 s) and 1 s (IT = 1 s) in a-b) and in c-d) respectively; inset on the left: scaled SERS spectra by peak amplitude at 1180 cm^{-1}, steady state temperature rise at the laser spot ΔT_{ls}^{SS} indicated in purple; inset on the right: temporal evolution of peak amplitude at 1180 cm^{-1} scaled by its maximum initial value, the corresponding decay rates α are indicted in brown (obtained by fitting with an exponential function). e-g) The temperature rise acquired during laser illumination, $\Delta T_{1\,\mathrm{mm}} = T_{1\,\mathrm{mm}} - T_a$ as a function of time for various laser powers P and flow rates Q.

similarly to the analysis conducted in [51], the observed difference in the double peak ∼1600 cm^{-1}, as a function of the laser power and flow rate, is attributed to the nature

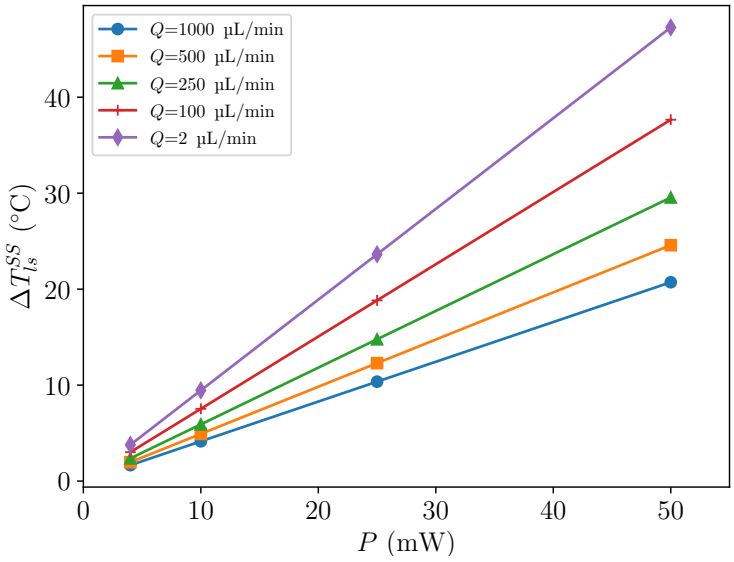

Figure 5: Steady state temperature increase at the laser spot ΔT_{ls}^{SS} as a function of laser power P and for several flow rates Q.

(type of symmetry) of vibration modes and to their specific dependence on temperature.

Changes in shape of the SERS spectra, at other Raman shifts, are visible for the other cases and their number increases with the temperature increase. For the same power as previously, $P = 4$ mW, but using a lower flow rate, $Q = 2$ μL/min, that induces a higher temperature increase, $\Delta T_{ls}^{SS} = 3.8$°C, additional slight changes are visible near 550, 850, 970, 1150 and 1300 cm^{-1}, inset (on the left) of Fig. 4d. Increasing again ΔT_{ls}^{SS}, reaching 20.7°C for $P = 50$ mW and $Q = 1000$ μL/min, leads to additional changes near 800 and 750 cm^{-1}, inset (on the left) of Fig. 4a. For the highest heating measured, $\Delta T_{ls}^{SS} \approx$50°C for $P = 50$ mW and $Q = 2$ μL/min, the shape of the SERS spectra is also affected near 700, 1400 and 1500 cm^{-1}, inset (on the left) of Fig. 4b.

It could be argued that the observed variations of the SERS signal (in terms of shape and intensity), during laser illumination, can come either from the degradation of the SERS substrate or from the photodegradation (or photobleaching) of probed molecules (CV). This cannot be attributed to the degradation of the SERS substrate because in this case, the modifications would be irreversible whereas this is not the case (several measurements have been made using the same zone of the SERS substrate).

Concerning the possible formation of bubbles, for the presented experiments, this has not been observed. Note that this is consistent with the maximum temperature reached $T_{ls}^{SS} = 70$ °C (< 100 °C) as measured in this work. Indeed, bubble formation has been encountered when no flow was applied (no cooling effect) and using the maximum

laser power. In this latter situation, bubbles formation (ebullition) induces fast and non-monotonic variations of the SERS signal (not shown).

Photodegradation of dyes, such as CV, is possible from the direct interaction of visible light with the molecules, but this generally requires a *sensitizer* (a source of O_2 enabling oxidation of the dye, such as methylene blue, benzophenone or dissolved O_2 in the case of CV) [52]. The corresponding kinetics are rather slow and nanoscale photocatalysts are used to speed up the process [53]. Here, the SERS substrate can play the role of the nanoscale photocatalyst during laser illumination. However, in this case, the changes in SERS spectra should depend on the laser power (magnitude of photon flux). This is not what is observed, the variations in SERS spectra are found to depend more on the local temperature than on laser power (for the same laser power, both the number of changes in SERS spectra and the variation of their intensity are found to depend on the flow rate used that influences the local temperature by inducing a cooling effect).

Furthermore, the photodegradation of CV leads to the formation of by-products as studied by chemical analyses (HPLC and UV-Vis spectroscopy) by Confortin et al. [54] or even by SERS [50]. The production of such molecules at the surface of the SERS substrate leads to significant changes in the SERS spectra (detection of by-products leading to new peaks); this has already been observed by Yang et al. [38] where specific Au@CdS core-shell nanocomposites were synthesized and used simultaneously as SERS substrate and photocatalyst (bifunctional nanomaterial). Here, no such significant changes are observed in the SERS spectra during a SERS measurement, the five main peaks of CV still appear in the acquired spectra (800, 950, 1180, 1380 and 1600 cm^{-1}). The observed slight changes in the shape of the SERS spectra (highlighted by the insets, on the left, of Fig. 4a, b, d) can be attributed to specific temperature dependencies such as for the the double peak at 1600 cm^{-1}.

The same trend is observed concerning the intensity decrease of SERS spectra, as shown by the insets (on the right) of Fig. 4a-d. From these graphs, the intensity loss correlates with the temperature increase ΔT_{ls}^{SS}: 25% (Fig. 4c), 50% (Fig. 4d), 50% (Fig. 4a) and 75% (Fig. 4b) for respectively 1.7 (Fig. 4c), 3.8 (Fig. 4d), 20.7 (Fig. 4a) and 47.3°C (Fig. 4b). Consequently, it is concluded that the CV is not photodegradated during the SERS measurement. Instead, the intensity decrease of SERS spectra is attributed to the thermal desorption of CV from the surface of the SERS substrate. This justified because the intensity of SERS spectra I_{SERS} is linked (proportional) to the adsorbed concentration of CV c_{ads} (Eq. 1).

Thermal desorption to explain the observed decrease of the SERS signal

It is well known that the increase of the temperature leads to the desorption of adsorbed molecules, i.e. the decrease of c_{ads} (keeping the concentration in the liquid phase constant) [55]. This dynamics can be modeled by the following mass balance at the surface

of the SERS substrate (assuming dilute solutions):

$$\frac{dc_{ads}}{dt} = k_{ad} c_{ads}^{sat} c(t,x,y,z=0) - k_{de} c_{ads}, \tag{3}$$

where k_{ad} and k_{de} are respectively the adsorption and desorption rate constants and c_{ads}^{sat} the saturation (maximum) surface concentration and $c(t,x,y,z=0)$ the concentration of CV at the surface of the SERS substrate. k_{ad} and c_{ads}^{sat} almost do not depend on temperature, unlike k_{de} which is given by:

$$k_{de} = \tau^{-1} e^{-Q_{ads}/(RT)}, \tag{4}$$

where τ^{-1} is a frequency related to molecular vibrations close the surface in absence of specific interactions, Q_{ads} the heat of adsorption, T the temperature and R is the ideal gas constant [55]. During a SERS measurement, the temperature increases that should lead to an increase in k_{de} (Eq. 4) and thus to the decrease of c_{ads} (Eq. 3). The measured decay rate of the intensity of the SERS signal, α, is indicated in each inset (on the right) of Fig 4a-d. A steady state is reached and the resulting adsorbed concentration is given by $c_{ads} = \frac{k_{ad} c_{ads}^{sat}}{k_{de}(T_{ls}^{SS})} c$, where c is the concentration of the used CV solution (10^{-6} M here). Consequently, the laser-induced temperature increase is expected to act on both the decay rate and the intensity loss of the SERS signal.

By assimilating the decay rates of the SERS signal, α, to the desorption rate constants, k_{de}, it is possible to estimate the value of Q_{ads} using the equation:

$$Q_{ads} = R \frac{\log\left(\frac{\alpha(50\text{ mW},Q)}{\alpha(4\text{ mW},Q)}\right)}{\frac{1}{T_{ls}^{SS}(4\text{ mW},Q)} - \frac{1}{T_{ls}^{SS}(50\text{ mW},Q)}}. \tag{5}$$

The thus obtained value of Q_{ads} is found to be dependent on the liquid flow rate Q: 13 and 92 kJ/mol for Q = 2 and 1000 μL/min respectively. This flow dependency shows that other acting mechanisms are not taken into account in this analysis based solely on adsorption-desorption.

Indeed, during laser illumination, the dynamics of the SERS signal depends on the coupling between adsorption-desorption, mass transfer by convection between the surface and the liquid phase as well as the heat transfer in the system.

In fact, the measured decay rates of I_{SERS} show well the competition between the kinetics of adsorption-desorption and the kinetics of mass transfer by convection as a function of temperature at the laser spot. At high laser power, i.e. at high temperature of the probed region, the kinetics of desorption is expected to be fast (high value of k_{de}, Eq. 4) but the removal of the molecules from the surface toward the liquid is ultimately limited by mass transfer by convection. In the latter case, the variation dynamics of c_{ads}, or in other terms the decay rate of I_{SERS}, should depend on the flow rate. On the

contrary, at low laser power, i.e. at temperature of the probed region close to T_a, the kinetics of desorption is expected to be slow (low value of k_{de}) and the removal of the molecules is not expected to be limited by convection. The decay rate of I_{SERS} should therefore depend less on the flow rate and ultimately being independent on it in the limit of high flow rates.

The experimentally measured decay rate α depends effectively more on the flow rate when a laser power P of 50 mW is used (0.21 and 3.27 s^{-1} for 2 and 1000 μL/min respectively, ratio of 15) than when P = 4 mW (0.11 and 0.33 min^{-1} for 2 and 1000 μL/min respectively, ratio of 3).

Note also the non monotonous variation of the intensity for $P = 50$ mW and $Q = 1000$ μL/min (inset, on the right, of Fig. 4a), where I_{SERS} reaches a minimum value before re-increasing. Such a dynamics could be due to the very fast variation of the temperature T_{ls} in that case (variation rate for $\Delta T_{1\,\mathrm{mm}} > 2$ s^{-1} as previously discussed) leading to a probably too fast depletion of adsorbed CV at the surface to be compensated by the convection mass flux (supply of CV); note also that this local temperature increase can also be too fast for the heat diffusion inside the bottom glass plate and the liquid.

To avoid a too complex analysis, here, these effects are not taken into account; a complete modelling of the SERS signal dynamics will be addressed in a future work.

Let's return to the estimation of Q_{ads}. The value of Q_{ads} obtained with the fastest flow, 92 kJ/mol, is excepted to be close to the right value. This is explained by the fact that in this case, the mass transfer by convection and heat transfer are fast and thus non limiting and consequently the current analysis, based solely on adsorption-desorption, should apply. This value, higher than 40 kJ/mol, indicates that the adsorption process is indeed a chemisorption process. A similar value ∼80 kJ/mol was obtained in the work of Satapathy et al. [56] in which the adsorption of CV on Ag nP was studied. This suggests a specific interaction between CV and nanoscale silver. This also validates the proposed effect of thermal desorption to explain the observed decrease of the SERS signal.

Effect of laser-induced heating on intensity of the SERS signal

During a SERS measurement, under laser illumination, once the steady state is reached, $dc_{ads}/dt = 0$, from Eq. 1, 3 and 4, the intensity of the SERS signal I_{SERS} is expected to be given by:

$$I_{SERS} = \left[A_{SERS}(w) k_{ad} c_{ads}^{sat} \tau c\right] . e^{Q_{ads}/(RT_{ls}^{SS})} . P.IT. \tag{6}$$

From this latter equation, I_{SERS} is expected to depend on T_{ls}^{SS}. As a consequence, at low laser powers and high flow rate, or in other terms low temperature increases, I_{SERS}/IT is expected to not be dependent on the flow rate Q ($T_{ls} \approx T_a$ and c_{ads} is constant). This is indeed verified in Fig. 6, where I_{SERS}/IT is plotted as a function of P for several values of Q. In the limit of low laser powers ($P \to 0$), the curves of each flow rate (in the range [2, 1000 μL/min]) get closer and tend to coincide. Furthermore, at low P,

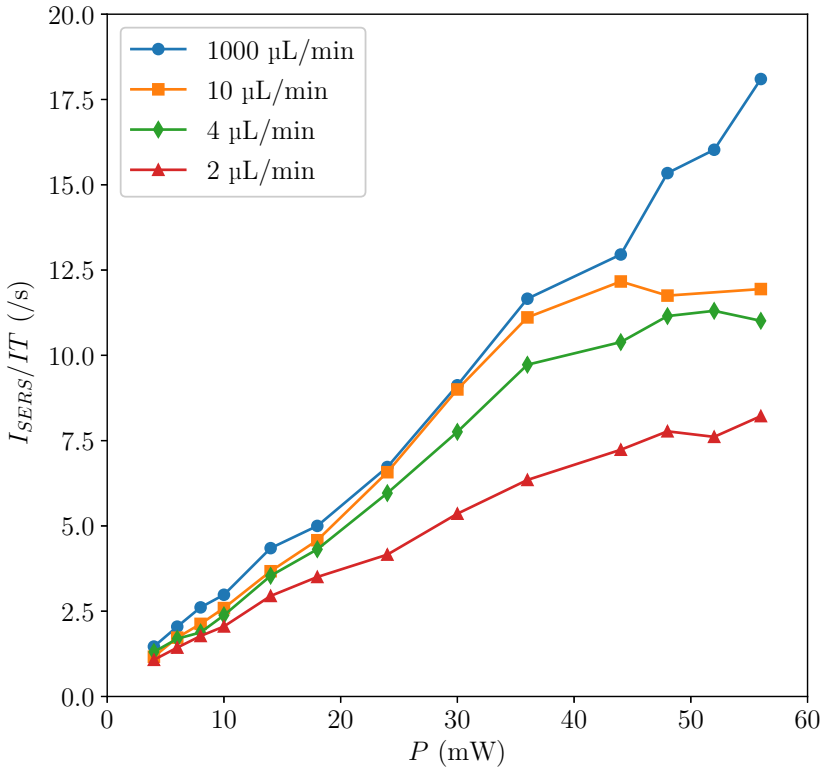

Figure 6: Steady state intensity of SERS spectra of a 10^{-6} M CV solution, divided by the integration time IT, as a function of the laser power P and for several flow rates Q. IT was varied in order to maximize the acquired SERS signal (extreme values: IT = 1 s for P = 4 mW, IT = 0.1 s for P = 55 mW). SERS spectra acquired after 1 min of laser illumination.

the corresponding signal I_{SERS}/IT evolves linearly with P that is in agreement with Eq. 6. By increasing P, the signal continues to increase with P but more slowly depending of the used flow rate. At the lower the flow rate, at least the signal intensity increases rapidly with P. For a given flow rate, there is a laser power threshold (optimum) beyond which the increase in SERS signal, by the increase in laser power, is no longer strong enough to compensate for the decrease in the adsorbed concentration because of laser-induced heating. The corresponding laser power threshold increases with the flow rate.

Note also that the linear dependence of I_{SERS} with the concentration c, as predicted by Eq. 6, is experimentally verified, see section 2 of SM.

3.1.2 Reversibility

The reversibility of the SERS measurement is evaluated by varying the CV concentration of the injected solution. The corresponding evolution of the intensity of the SERS spectra, by cycling CV concentrations, starting at 10^{-8} to 10^{-6} M then decreased to 10^{-8} M and using a flow rate Q = 6.5 μL/min, is shown if Fig. 7. When using a laser

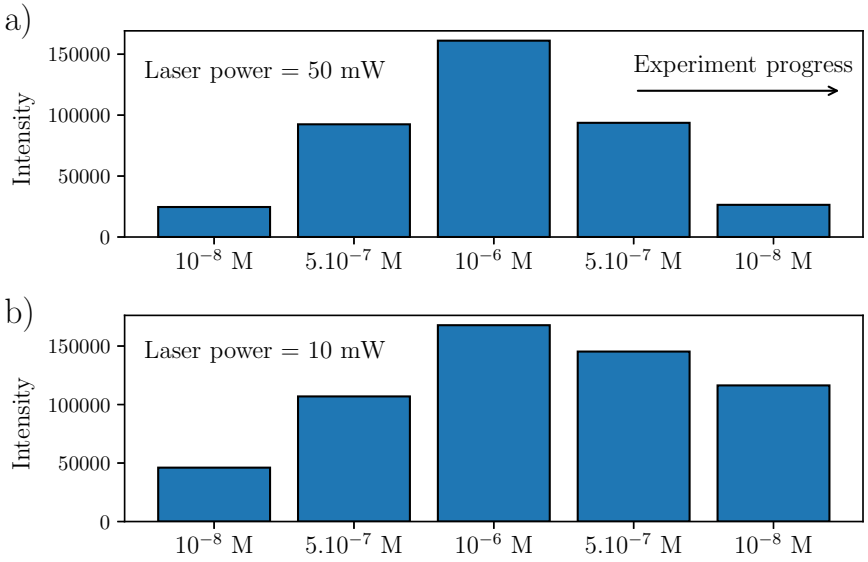

Figure 7: Intensity of SERS spectra (acquired after 1 min of laser exposure) of CV solutions at different concentrations (indicated by the horizontal axis of the graph) and flowing at Q = 6.5 μL/min in the main microchannel (no gradients). Experiment progress is from left to right (indicated by the arrow in a)); The CV concentration is first increased, starting at 10^{-8} to 10^{-6} M, then decreased to 10^{-8} M. a) Laser power = 50 mW, b) laser power = 10 mW.

power of 50 mW, Fig. 7a, the intensity of SERS spectra follows the evolution of CV concentration in the main microchannel, whatever the order of the injected solutions. The measurement is effectively reversible. This result is consistent with the previous analysis since the same dynamics (decay rates) are expected here, ensuring a stable (steady state) SERS signal in less than 1 min (the SERS measurement time used).

However, when using a lower laser power, of 10 mW, after contact of the SERS substrate with a 10^{-6} M solution, when the CV concentration is decreased, the intensity of the SERS spectra (after 1 min of laser illumination) does not return to the values obtained in the initial phase of increasing concentration (from 10^{-8} to 10^{-6} M), Fig. 7b.

It can be concluded that, for low laser powers, when the CV concentration is de-

creased, there remains an excess adsorbed CV molecules, coming from exposure to the previous solution more concentrated in CV. During the measurement time used (1 min), the laser-induced heating is not high enough to allow a fast enough thermal desorption which would allow the return to the values obtained for the increasing concentration phase.

Furthermore, for these situations, where a SERS measurement is performed after a decrease in CV concentration, the decay rates of the SERS intensity are found to be lower than for the previous situations where the flowing solution contained CV at a constant concentration (10^{-6} M, as in the previous part); for the ultimate case where the SERS substrate, previously exposed to a 10^{-6} M solution, is exposed to a CV-free solution ($c = 0$), e.g. for P = 50 mW and Q = 1000 μL/min, decay rate ≈ 0.24 s^{-1} instead of 3.27 s^{-1} when $c = 10^{-6}$ M and for P = 10 mW, decay rate ≈ 0.8 min^{-1} and 0.4 min^{-1} for Q = 1000 and 10 μL/min respectively.

These slower dynamics can also be explained by the mass transfer of CV by convection in the liquid. Indeed, even if a flow is applied, the removal of the desorbed CV is limited by the convection flux leading to an accumulation of CV in the liquid at the surface of the SERS substrate and thus to a positive (non-zero) value of the concentration $c(t,x,y,z = 0)$. This latter value induces a non-zero adsorption term in the right hand side of Eq. 3 and thus a slowed decrease of c_{ads} and a longer time to reach the steady state. This effect is all the more pronounced as the local fluid velocity is very low (velocity = 0 at the wall).

Here, we exploit this efficient thermal desorption, at high laser power (50 mW), to regenerate the surface of the SERS substrate. The laser at high power can thus be used as an "eraser" to remove the traces of CV from a previous experiment and come back to a base state.

Note that after erasing a given location/point, after a period of some minutes without laser illumination, in water without CV, the SERS signal is partially restored. This is indeed attributed to diffusion of CV, from the surface surrounded the targeted location (by surface diffusion and/or by desorption followed by diffusion and re-adsorption); by also erasing around the targeted location, signal restoration is limited.

To sum up, these results show that the coupling between adsorption, mass transfer and heat transfer plays an important role on the dynamics of the SERS signal and should be taken into account to optimize the SERS signal in terms of intensity and reversibility.

3.1.3 Enhancement

To evaluate the enhancement provided by the SERS substrate, the normal Raman spectrum of CV is measured in another Y-shaped microfluidic chip which has the same geometry as the SERS microfluidic chip but in which no SERS substrate has been integrated, see the blue dashed line in Fig. 8. Note also that this latter spectrum is obtained with a more concentrated solution of CV (10^{-3} M) and a higher IT (1.0 s) than for

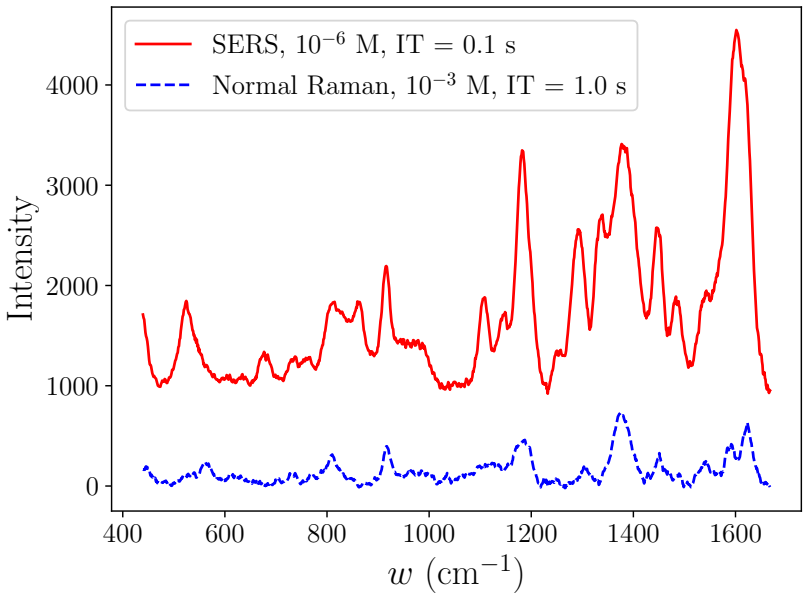

Figure 8: Steady state SERS (red solid line) and normal Raman (blue dashed line) spectra of CV (after baseline subtraction) obtained respectively in the SERS microfluidic chip, with a concentration of 10^{-6} M and an integration time (IT) of 0.1 s and in another microfluidic chip which the geometry is the same as the SERS microfluidic chip, but without SERS substrate (normal Raman), with a concentration of 10^{-3} M and an IT of 1.0. Q = 1000 μL/min, laser power = 50 mW, SERS spectrum acquired after 1 min of laser illumination.

SERS measurements. Note that the normal Raman spectrum is not subject to variations and does not depend on the flow rate.

The steady state SERS spectrum of CV, obtained with the same laser power (P = 50 mW, and a flow rate Q of 1000 μL/min), but with a CV concentration of 10^{-6} M and IT = 0.1 s, is shown by the red solid line in Fig. 8. As expected, the same main peaks are obtained in normal Raman and SERS spectra.

From these data, the AEF can be estimated using Eq. 2 in which the signal intensities are corrected to take into account the different values of IT (IT_{SERS} = 0.1 s, IT_{Raman} = 1.0 s):

$$\mathrm{AEF} = \frac{(I_{SERS}/IT_{SERS})/c_{SERS}}{(I_{Raman}/IT_{Raman})/c_{Raman}}. \tag{7}$$

Considering the peak at 1180 cm^{-1}, the intensities of the SERS and normal Raman spectra, I_{SERS} and I_{Raman}, correspond roughly to 2500 and 500 (a.u.) respectively. This leads to an AEF of 5×10^4 which shows that the Raman signal is really enhanced by the electrodeposited SERS substrate. Note that the real value of AEF is indeed higher

because of the initial thermal desorption of CV. From the intensity loss for the present case (50 mW, 1000 μL/min), evaluated at 50% (inset, on the right, of Fig. 4a), the real value of AEF of the electrodeposited SERS substrate is 10^5.

3.1.4 Spatial uniformity

The spatial uniformity of the SERS substrate is evaluated by making the same measurements, as in the previous subsections, at several points. In Fig. 9, the relative spatial variation of SERS signal intensity I, $I/\langle I\rangle - 1$ (where $\langle I\rangle$ is the average value of I), is plotted along the y-axis (Fig. 9a) and along the x-axis (Fig. 9b); y-axis is oriented perpendicular to the flow and x-axis is oriented parallel to the flow, as sketched in Fig. 1a-c and Fig. 3a.

Along both y and x axis, the RSD and RAV of the SERS signal is $<7\%$ and $<13\%$ respectively (Fig. 9). These values are within the ranges of RSD and RAV reported in other works, Table 1. Specifically along the x-axis, the variations are oscillating, and the corresponding period, $\sim$650 μm (from FFT processing), correlates well with the average lateral size (width) of the finger-shaped and rounded deposit structures (separated by dark zones) as observed by SEM, Fig. 3a. Consequently, the non-uniformity of the nanostructure leads to the non-uniformity of the SERS signal. However, it has to be noted that, here, the spatial variation of SERS signal remains low and in the range of other works. The fact that a not so bad enhancement is measured on the "dark zones", which contain larger and less sharp structures than in other regions of the SERS substrate (Fig. 3), could be explained by the large size of the laser spot (192 μm, Gaussian width in terms of $1/e^2$) compared to the size/width of these dark zones $\sim$20 μm, as seen in magnified SEM images (Fig. 3c). In this way, the bad enhancement in the dark zones contributes only to a small part of the total scattered light. Note that the spatial resolution of the SERS measurement is unknown (not measured) but can be expected to be approximately close to the standard deviation of the laser spot 49 μm.

In overall, a good uniformity of the SERS signal is obtained on a large surface area, of 1.5 mm $\times$ 2 cm, which is comparable to the largest surface area of SERS substrate fabricated so far [30], Table 1. Note that larger SERS substrates, or of controllable size and location, can be fabricated with the proposed method.

Concerning the stability of the devices produced, the experiments were carried out for 18 months with the same devices without observing any drop in their performance (in terms of AEF and uniformity). In agreement with the reproducibility of the nanostructure, the Raman enhancement (AEF) is found to be reproducible for all the devices produced (+/- 10%).

In the next section, the ability to image concentration gradients is evaluated.

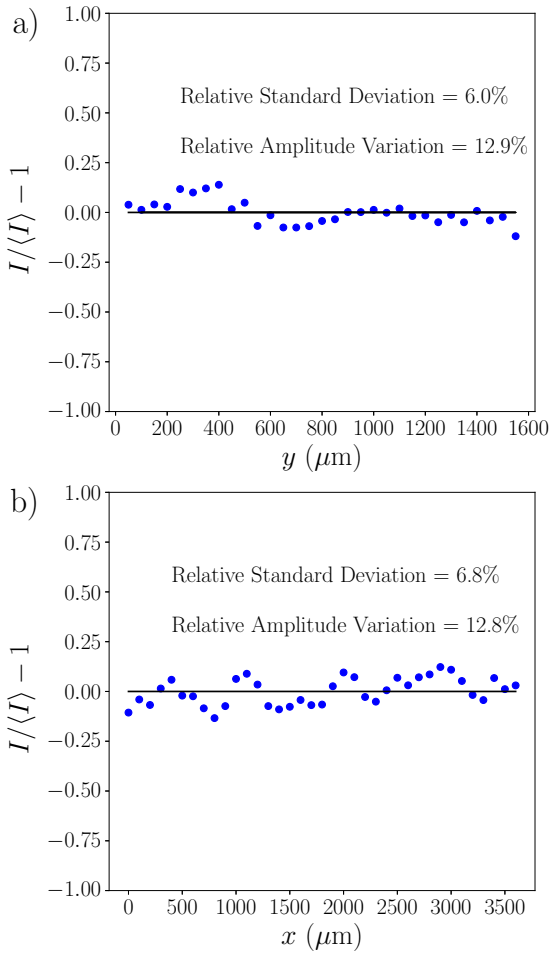

Figure 9: Relative spatial variations of the steady state SERS signal intensity (from the peak at 1180 cm^{-1}) along the x a) and y b) axis shown in Fig. 3a and Fig. 1a-c. Q = 1000 μL/min, CV concentration = $10^{-6}M$, laser power = 50 mW, IT = 0.1 s, SERS spectrum acquired after 1 min of laser illumination.

3.2 Imaging of concentration gradients

3.2.1 Optical profiles

Before attempting the SERS imaging of concentration gradients, the expected gradients are first observed optically in another Y-shaped microfluidic chip which has the same geometry as the SERS microfluidic chip but in which no SERS substrate has been integrated (as for previous normal Raman measurements). A transverse diffusion profile of CV is produced in the main microchannel by injecting a 5.10^{-4} M solution of CV in one inlet and water in the other. The use of CV at this concentration makes the gradi-

ent visible in the main microchannel (well lower concentration will be used for SERS). Some of the resulting gradients, taken at x = 2 cm from the contact between the two inlet microchannels (inlet of the main microchannel), are shown for various flow rates Q in the inset of Fig. 10a (note that Q is the total flow rate in the main microchannel). By assimilating the inverted greyscale of the images to the concentration of CV (the CV solution appears darker than water because of light absorption by CV), and after normalization, the normalized concentration profiles are shown for several flow rates in Fig. 10a (curves with markers). We obtain the usual S-shaped curves; the higher the flow rate, the steeper the profile.

If the diffusion along the depth of the main microchannel (z-axis) is sufficiently fast, compared to the one along the transverse direction (y-axis), the concentration field can be considered two-dimensional (the local concentration c does not depend on z) and the solution of the advection-diffusion problem [3] is given by:

$$c(y,x) = \frac{1}{2}\left(\text{erf}\left(\frac{y-y_0}{\delta(x)}\right)+1\right), \tag{8}$$

where y_0 is the center of the gradient and $\delta(x) = \sqrt{\frac{4x}{u}D}$, with u the mean flow velocity in the main microchannel ($u = Q/(h_l W)$) and D the diffusion coefficient of CV, the width of the gradient, or the diffusion length after the duration of one local residence time $\frac{4x}{u}$. The deviation from this two-dimensional situation appears for fast flows, in thick and long microchannels, and this leads to enhanced diffusion in the vicinity of upper and bottom walls compared to the center of the microchannel [1, 57]. From 3D numerical simulations of the advection-diffusion problem in the main microchannel, it was verified that the concentration field can be effectively considered two-dimensional, and thus Eq. 8 applies, for $Q \leq 250$ μL/min (see section 3 of SM) and thus for all the profiles shown in Fig. 10a. In Fig. 10a, the experimental profiles are fitted with the theoretical relationship Eq. 8 (red solid curves). The obtained values of δ are plotted as a function of $\sqrt{\frac{4x}{u}}$ in Fig. 10b. The values of δ follow very well the square root law and for D a value of 3.140×10^{-10} m^2/s is measured for CV with this optical technique.

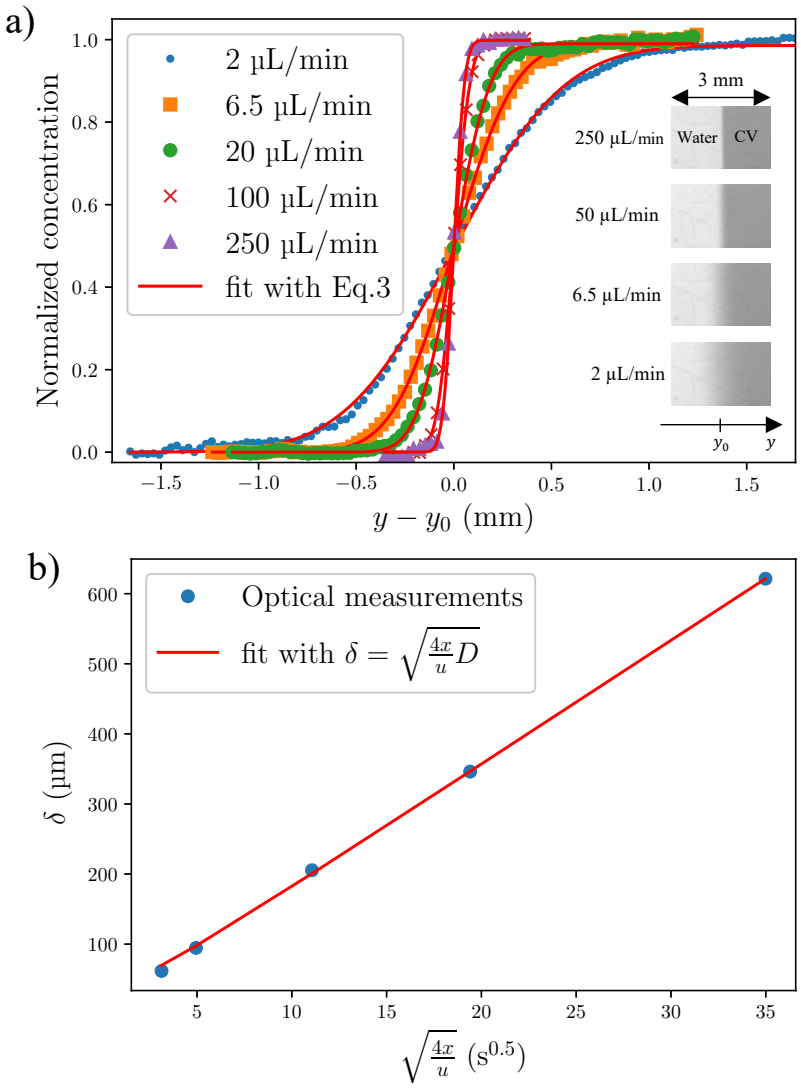

Figure 10: a) Normalized concentration profiles along the width of the main microchannel for several flow rates and at a distance $x = 2$ cm from the inlet of the main microchannel (for clarity purposes, only one point out of six is shown), the red curves correspond to Eq. 8 adjusted on the experimental points, inset: images of the concentration gradients. b) Plot of the width of the gradients δ, determined from the fit of experimental data of a) with Eq. 8, as a function of the square root of the local residence time $\frac{4x}{u}$.

3.2.2 SERS profiles

Now, the imaging of concentration gradients is attempted by SERS. The transverse diffusion profiles of CV are produced by injecting a 10^{-6} M solution of CV, in the inlet

of the side opposed to the SERS substrate, and a 10^{-8} M solution of CV in the other inlet, as sketched in Fig. 1a. Note that the solution at 10^{-6} M is completely transparent in the chip, so observations of gradients based on optical absorption are no longer possible. The flow rates are adapted to bring the center of the gradient at mid length of the SERS substrate. At a distance x = 1.7 cm from the inlet of the main microchannel, SERS spectra are recorded at several points across the width of the main microchannel by using the manual micrometric translation stage along the y-axis (steps of 50 μm). The laser power used is 50 mW and the SERS spectra are acquired after 1 min of laser

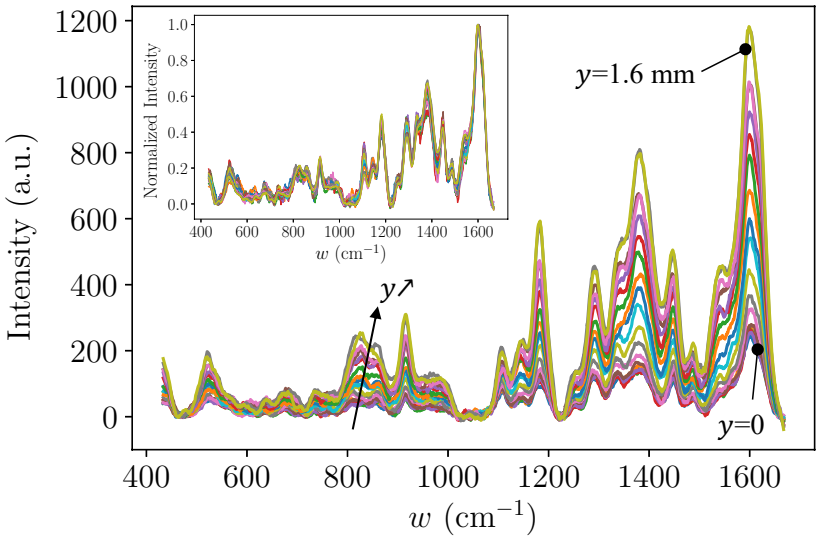

Figure 11: SERS spectra (after baseline subtraction) measured at several transverse locations y (steps of 50 μm), and at x = 1.7 cm from the inlet of the main microchannel, in the presence of a concentration gradient produced by the continuous injection of a CV solution at 10^{-6} M, in the inlet opposed to the SERS substrate, and of a CV solution at 10^{-8} M in the other inlet of the chip for a total flow rate Q of 6.5 μL/min. Inset: SERS spectra scaled by their maximum value. Laser power = 50 mW, IT = 0.1 s, SERS spectra acquired after 1 min of laser illumination.

illumination that enables a reversible measurement (according the previous part) whatever the spatiotemporal variations of CV concentration in the chip, notably when the transverse diffusion profiles are varied. For a flow rate Q of 6.5 μL/min, the obtained SERS spectra are shown in Fig. 11. The spectra measured at low y values, i.e. in the low concentrated stream (10^{-8} M), have a low intensity whereas spectra measured further inside the main microchannel, in the more concentrated stream (10^{-6} M), exhibit a higher intensity. In the inset of Fig. 11, these spectra are shown after being scaled by their maximum value. All scaled SERS spectra coincide well. This shows that CV is detected efficiently even at a concentration of 10 nM (even if this is not the major con-

cern here, a limit of detection ∼5 nM has been estimated for CV, see below and section 2 of SM). The intensity of the SERS spectra is quantified from the intensity of the peak at 1180 cm^{-1}. After normalization, the intensity profiles are shown in Fig. 12 (curves with markers) for several flow rates Q in the range [6.5, 1000 μL/min].

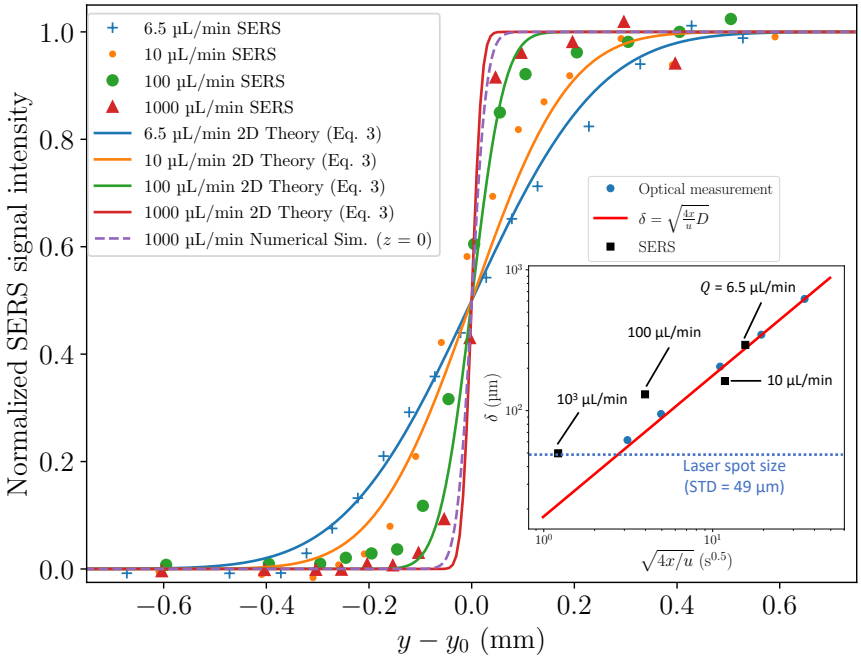

Figure 12: Curves with markers: normalized intensity profiles of SERS spectra along the width of the microchannel for several flow rates Q and at a distance $x = 1.7$ cm from the inlet of the main microchannel (the intensity of the SERS spectra is measured by the intensity of the peak at 1180 cm^{-1}), solid lines: normalized concentration profiles predicted by the 2D theory (Eq. 8) using $x = 1.7$ cm and $D = 3.140\times10^{-10}$ m^2/s (obtained by the optical method, Fig. 11), dashed line: normalized concentration profile at the SERS substrate surface ($z = 0$ and $x = 1.7$ cm) from numerical simulation (section 3 of SM) for Q = 1000 μL/min; inset : plot of the width of the gradients δ, black squares for SERS measurements (determined by adjusting Eq. 8 on experimental points of the SERS profiles) and blue disks for optical measurements (Fig. 10b), as a function of the square root of the local residence time $\frac{4x}{u}$, the red solid line corresponds to the plot $\delta = \sqrt{4xD/u}$ and the blue dotted line indicates the size of the laser spot in terms of standard deviation (49 μm). Laser power = 50 mW, IT = 0.1 s, SERS spectra acquired after 1 min of laser illumination.

The normalized concentration profiles, predicted by Eq. 8 at the same distance from the inlet of the main microchannel $x = 1.7$ cm and using the value of the diffusion

coefficient determined optically (D = 3.140×10^{-10} m^2/s), are also shown in the same graph (solid lines).

For $Q \leq 100$ μL/min, the concentration field is two-dimensional and the concentration at the surface of the SERS substrate ($z = 0$), is the same as at mid-depth ($z = h_l/2$) of the main microchannel at a given couple of coordinates x and y. Therefore the concentration profiles obtained from the 2D theory should match the SERS profiles (since I_{SERS} is proportional to c, section 1.2). As shown in Fig. 12, the SERS profiles indeed coincide well with the concentration profiles. For the highest flow rate used of 1000 μL/min, the numerical simulation shows a non-negligible deviation from the two-dimensionality (section 3 of SM). Consequently, for $Q = 1000$ μL/min, the SERS profile is not expected to match the concentration profile predicted by the 2D theory (Eq. 8). This is what is actually observed in Fig. 12. For this high flow rate, the SERS profile should match the concentration profile at the SERS substrate surface ($z = 0$) provided by the numerical simulation and shown by the dashed line in Fig. 12. However, the gap between this latter profile, at the SERS substrate surface, and the profile from the 2D theory is low and the SERS profile remains away from the real concentration profile.

This gap is more easily visible in the inset of Fig. 12, where the width of the gradients (diffusion length) δ, obtained by fitting the SERS profiles with Eq. 8 (black squares), is plotted as a function of $\sqrt{\frac{4x}{u}}$ for the various flow rates Q; the same plot for the optical measurement, and thus for the real 2D concentration profiles (for low Q), is also shown (blue disks and red solid line). For low flow rates (from 6.5 to 100 μL/min), δ values obtained by SERS are close to the real ones (mean gap = 37%) while for $Q = 1000$ μL/min a significant gap of 130% is measured. This is explained by the low gradient width for this flow rate (24 μm) which is probably too low compared to the resolution of the SERS measurement performed with a rather large laser spot which the standard deviation is 49 μm; this size is also shown in the inlet of Fig. 12.

To sum up, for the wide range of investigated flow rates, the SERS profiles coincide well with the real concentration profiles, provided that Q is low enough to ensure a 2D concentration field. Transverse diffusion profiles are therefore quantitatively imaged by SERS for $Q \leq 100$ μL/min. Furthermore, this is done with weakly concentrated streams. This also suggests that the intensity of the SERS signal I_{SERS} is proportional to the (local) concentration, what is in agreement with other measurements where this linear dependence was verified by injecting solutions with different concentrations of CV, see section 2 of SM.

4 Conclusions

An adherent and uniform nanostructured silver layer was electrodeposited, in one step, over the bottom glass wall of a microchannel. This deposit is successfully tested as immobilized SERS substrate by inducing an analytical enhancement factor of 5.10^4 uniformly distributed (RSD $< 7\%$) over its large surface (2 cm $\times$ 1.5 mm). By integrating this SERS substrate in a Y-shaped chip, this good spatial uniformity was used to quantitatively image transverse diffusion concentration profiles by SERS. The SERS measurement is found to be reversible when using a sufficiently high laser power P. This is attributed to the laser induced heating (photothermal effect) which induces the thermal desorption of the probed molecules (CV) and a faster response of the signal when the concentration is changed (decreased notably). The SERS microfluidic chip proposed in this work is thus re-usable when using the right operating parameters in terms of laser power and flow rate. However, a too high laser heating (high ratio laser power/flow rate) induces an important depletion of adsorbed molecules and thus a decrease of SERS signal intensity. A compromise must be found between the response speed and the intensity of the SERS signal. This effect was highlighted thanks to the microfluidic configuration which allows to precisely and independently control the laser power, the concentration of probed molecules in the flowing liquid and the cooling of the SERS substrate by liquid flow. Finally, this study shows that the correct selection of these operating parameters is as important as the optimization of the SERS substrate itself. The consideration of all these aspects will contribute to the development of reversible and sensitive SERS-based chemical imaging in microfluidic devices to study and analyze chemical, biochemical or biological processes.

Conflicts of interest

There are no conflicts to declare.

Acknowledgements

This study was supported by the project PLUS ICARE of the Laboratoire de Génie Chimique (LGC). The author is very grateful to M. L. de Solan-Bethmale (LGC) for SEM observations.

References

[1] R. F. Ismagilov, A. D. Stroock, P. J. A. Kenis, G. Whitesides, and H. A. Stone, "Experimental and theoretical scaling laws for transverse diffusive broadening

in two-phase laminar flows in microchannels," *Applied Physics Letters*, vol. 76, pp. 2376–2378, 04 2000.

[2] A. E. Kamholz, E. A. Schilling, and P. Yager, "Optical measurement of transverse molecular diffusion in a microchannel," *Biophysical Journal*, vol. 80, no. 4, pp. 1967–1972, 2001.

[3] J.-B. Salmon, A. Ajdari, P. Tabeling, L. Servant, D. Talaga, and M. Joanicot, "In situ Raman imaging of interdiffusion in a microchannel," *Applied physics letters*, vol. 86, no. 9, p. 094106, 2005.

[4] W. D. Ristenpart, J. Wan, and H. A. Stone, "Enzymatic reactions in microfluidic devices: Michaelis- menten kinetics," *Analytical Chemistry*, vol. 80, no. 9, pp. 3270–3276, 2008.

[5] J.-B. Salmon, C. Dubrocq, P. Tabeling, S. Charier, D. Alcor, L. Jullien, and F. Ferrage, "An Approach to Extract Rate Constants from Reaction-Diffusion Dynamics in a Microchannel," *Analytical Chemistry*, vol. 77, no. 11, pp. 3417–3424, 2005.

[6] C. N. Baroud, F. Okkels, L. Ménétrier, and P. Tabeling, "Reaction-diffusion dynamics: Confrontation between theory and experiment in a microfluidic reactor," *Phys. Rev. E*, vol. 67, p. 060104, 2003.

[7] K. L. A. Chan, S. Gulati, J. B. Edel, A. J. de Mello, and S. G. Kazarian, "Chemical imaging of microfluidic flows using ATR-FTIR spectroscopy," *Lab on a Chip*, vol. 9, no. 20, pp. 2909–2913, 2009.

[8] K.-I. Miyamoto, A. Itabashi, T. Wagner, M. J. Schöning, and T. Yoshinobu, "High-speed chemical imaging inside a microfluidic channel," *Sensors and Actuators B: Chemical*, vol. 194, pp. 521–527, 2014.

[9] H. Keles, F. Susanne, H. Livingstone, S. Hunter, C. Wade, R. Bourdon, and A. Rutter, "Development of a robust and reusable microreactor employing laser based mid-ir chemical imaging for the automated quantification of reaction kinetics," *Organic Process Research & Development*, vol. 21, no. 11, pp. 1761–1768, 2017.

[10] A. Kara, A. Reitz, J. Mathault, S. Mehou-Loko, M. A. Amirdehi, A. Miled, and J. Greener, "Electrochemical imaging for microfluidics: a full-system approach," *Lab on a Chip*, vol. 16, no. 6, pp. 1081–1087, 2016.

[11] G. Cristobal, L. Arbouet, F. Sarrazin, D. Talaga, J.-L. Bruneel, M. Joanicot, and L. Servant, "On-line laser raman spectroscopic probing of droplets engineered in microfluidic devices," *Lab on a Chip*, vol. 6, no. 9, pp. 1140–1146, 2006.

[12] E. Fradet, C. Bayer, F. Hollfelder, and C. N. Baroud, "Measuring fast and slow enzyme kinetics in stationary droplets," *Analytical Chemistry*, vol. 87, no. 23, pp. 11915–11922, 2015.

[13] P. Zhou, H. He, H. Ma, S. Wang, and S. Hu, "A review of optical imaging technologies for microfluidics," *Micromachines*, vol. 13, no. 2, p. 274, 2022.

[14] C. L. Haynes, A. D. McFarland, and R. P. Van Duyne, "Surface-Enhanced Raman Spectroscopy," *Analytical Chemistry*, vol. 77, no. 17, pp. 338 A–346 A, 2005.

[15] F. Paquet-Mercier, N. B. Aznaveh, M. Safdar, and J. Greener, "A microfluidic bioreactor with in situ SERS imaging for the study of controlled flow patterns of biofilm precursor materials," *Sensors*, vol. 13, no. 11, pp. 14714–14727, 2013.

[16] G. Barbillon, C. Humbert, M. U. González, and J. M. García-Martín, "Gold nanocolumnar templates for effective chemical sensing by surface-enhanced raman scattering," *Nanomaterials*, vol. 12, no. 23, p. 4157, 2022.

[17] R. Panneerselvam, H. Sadat, E.-M. Höhn, A. Das, H. Noothalapati, and D. Belder, "Microfluidics and surface-enhanced raman spectroscopy, a win–win combination?," *Lab on a Chip*, vol. 22, no. 4, pp. 665–682, 2022.

[18] M. Fan, G. F. Andrade, and A. G. Brolo, "A review on the fabrication of substrates for surface enhanced raman spectroscopy and their applications in analytical chemistry," *Analytica chimica acta*, vol. 693, no. 1-2, pp. 7–25, 2011.

[19] Y.-J. Oh and K.-H. Jeong, "Optofluidic SERS chip with plasmonic nanoprobes self-aligned along microfluidic channels," *Lab on a Chip*, vol. 14, no. 5, pp. 865–868, 2014.

[20] B.-B. Xu, Z.-C. Ma, L. Wang, R. Zhang, L.-G. Niu, Z. Yang, Y.-L. Zhang, W.-H. Zheng, B. Zhao, Y. Xu, *et al.*, "Localized flexible integration of high-efficiency surface enhanced raman scattering (SERS) monitors into microfluidic channels," *Lab on a Chip*, vol. 11, no. 19, pp. 3347–3351, 2011.

[21] A. Gopalakrishnan, M. Chirumamilla, F. De Angelis, A. Toma, R. P. Zaccaria, and R. Krahne, "Bimetallic 3D Nanostar Dimers in Ring Cavities: Recyclable and Robust Surface-Enhanced Raman Scattering Substrates for Signal Detection from Few Molecules," *ACS Nano*, vol. 8, no. 8, pp. 7986–7994, 2014.

[22] C. Li, Y. Huang, X. Li, Y. Zhang, Q. Chen, Z. Ye, Z. Alqarni, S. Bell, and Y. Xu, "Towards practical and sustainable SERS: a review of recent developments in the construction of multifunctional enhancing substrates," *Journal of Materials Chemistry C*, pp. 11517–11552, 2021.

[23] P. A. Mosier-Boss, "Review of SERS substrates for chemical sensing," *Nanomaterials*, vol. 7, no. 6, p. 142, 2017.

[24] L. Chen and J. Choo, "Recent advances in surface-enhanced raman scattering detection technology for microfluidic chips," *Electrophoresis*, vol. 29, no. 9, pp. 1815–1828, 2008.

[25] T. Ge, S. Yan, L. Zhang, H. He, L. Wang, S. Li, Y. Yuan, G. Chen, and Y. Huang, "Nanowire assisted repeatable DEP–SERS detection in microfluidics," *Nanotechnology*, vol. 30, no. 47, p. 475202, 2019.

[26] J. Plou, M. Charconnet, I. García, J. Calvo, and L. M. Liz-Marzán, "Preventing memory effects in surface-enhanced raman scattering substrates by polymer coating and laser-activated deprotection," *ACS nano*, vol. 15, no. 5, pp. 8984–8995, 2021.

[27] T.-A. Meier, E. Poehler, F. Kemper, O. Pabst, H.-G. Jahnke, E. Beckert, A. Robitzki, and D. Belder, "Fast electrically assisted regeneration of on-chip SERS substrates," *Lab on a Chip*, vol. 15, no. 14, pp. 2923–2927, 2015.

[28] E. C. Le Ru, E. Blackie, M. Meyer, and P. G. Etchegoin, "Surface enhanced raman scattering enhancement factors: a comprehensive study," *The Journal of Physical Chemistry C*, vol. 111, no. 37, pp. 13794–13803, 2007.

[29] M. Lafuente, I. Pellejero, A. Clemente, M. A. Urbiztondo, R. Mallada, S. Reinoso, M. P. Pina, and L. M. Gandía, "In situ synthesis of SERS-active Au@POM nanostructures in a microfluidic device for real-time detection of water pollutants," *ACS applied materials & interfaces*, vol. 12, no. 32, pp. 36458–36467, 2020.

[30] S.-J. Lin, P.-H. Chao, H.-W. Cheng, J.-K. Wang, Y.-L. Wang, Y.-Y. Han, and N.-T. Huang, "An antibiotic concentration gradient microfluidic device integrating surface-enhanced raman spectroscopy for multiplex antimicrobial susceptibility testing," *Lab on a Chip*, vol. 22, no. 9, pp. 1805–1814, 2022.

[31] R. G. Freeman, K. C. Grabar, K. J. Allison, R. M. Bright, J. A. Davis, A. P. Guthrie, M. B. Hommer, M. A. Jackson, P. C. Smith, D. G. Walter, *et al.*, "Self-assembled metal colloid monolayers: an approach to SERS substrates," *Science*, vol. 267, no. 5204, pp. 1629–1632, 1995.

[32] D. Lin, Z. Wu, S. Li, W. Zhao, C. Ma, J. Wang, Z. Jiang, Z. Zhong, Y. Zheng, and X. Yang, "Large-area Au-nanoparticle-functionalized Si nanorod arrays for spatially uniform surface-enhanced raman spectroscopy," *ACS nano*, vol. 11, no. 2, pp. 1478–1487, 2017.

[33] S. Li, N. Zhang, N. Zhang, D. Lin, X. Hu, and X. Yang, "Three-dimensional ordered Ag/ZnO/Si hierarchical nanoflower arrays for spatially uniform and ultrasensitive SERS detection," *Sensors and Actuators B: Chemical*, vol. 321, p. 128519, 2020.

[34] C. Wang, S. Zhou, Y. Tian, A. Jiao, H. Ma, M. Zhang, L. Zheng, X. Liu, Q. Cui, S. Li, *et al.*, "Super-hydrophilic SERS sensor with both ultrahigh activity and exceptional 3D spatial uniformity for sensitive detection of toxic pollutants," *Applied Surface Science*, vol. 603, p. 154445, 2022.

[35] M. Li, F. Zhao, J. Zeng, J. Qi, J. Lu, and W.-C. Shih, "Microfluidic surface-enhanced raman scattering sensor with monolithically integrated nanoporous gold disk arrays for rapid and label-free biomolecular detection," *Journal of biomedical optics*, vol. 19, no. 11, pp. 111611–111611, 2014.

[36] Z. Wang, S. Ye, N. Zhang, X. Liu, and M. Wang, "Triggerable mutually amplified signal probe based SERS-microfluidics platform for the efficient enrichment and quantitative detection of mirna," *Analytical chemistry*, vol. 91, no. 8, pp. 5043–5050, 2019.

[37] P. G. Etchegoin, P. D. Lacharmoise, and E. Le Ru, "Influence of photostability on single-molecule surface enhanced raman scattering enhancement factors," *Analytical Chemistry*, vol. 81, no. 2, pp. 682–688, 2009.

[38] J.-L. Yang, J. Xu, H. Ren, L. Sun, Q.-C. Xu, H. Zhang, J.-F. Li, and Z.-Q. Tian, "In situ SERS study of surface plasmon resonance enhanced photocatalytic reactions using bifunctional Au@ CdS core–shell nanocomposites," *Nanoscale*, vol. 9, no. 19, pp. 6254–6258, 2017.

[39] G. Baffou, J. Polleux, H. Rigneault, and S. Monneret, "Super-heating and microbubble generation around plasmonic nanoparticles under cw illumination," *The Journal of Physical Chemistry C*, vol. 118, no. 9, pp. 4890–4898, 2014.

[40] Z.-C. Zeng, H. Wang, P. Johns, G. V. Hartland, and Z. D. Schultz, "Photothermal microscopy of coupled nanostructures and the impact of nanoscale heating in surface-enhanced raman spectroscopy," *The Journal of Physical Chemistry C*, vol. 121, no. 21, pp. 11623–11631, 2017.

[41] T. Kang, S. Hong, Y. Choi, and L. P. Lee, "The effect of thermal gradients in SERS spectroscopy," *Small*, vol. 6, no. 23, pp. 2649–2652, 2010.

[42] M. D. King, S. Khadka, G. A. Craig, and M. D. Mason, "Effect of local heating on the SERS efficiency of optically trapped prismatic nanoparticles," *The Journal of Physical Chemistry C*, vol. 112, no. 31, pp. 11751–11757, 2008.

[43] K. W. Kho, Z. X. Shen, Z. Lei, F. Watt, K. C. Soo, and M. Olivo, "Investigation into a surface plasmon related heating effect in surface enhanced raman spectroscopy," *Analytical chemistry*, vol. 79, no. 23, pp. 8870–8882, 2007.

[44] C. Kharbachi, T. Tzedakis, and F. Chauvet, "Crossover between re-nucleation and dendritic growth in electrodeposition without supporting electrolyte," *Journal of The Electrochemical Society*, vol. 168, no. 7, p. 072507, 2021.

[45] V. Fleury, W. A. Watters, L. Allam, and T. Devers, "Rapid electroplating of insulators," *Nature*, vol. 416, pp. 716–719, 2002.

[46] V. Fleury, "Branched fractal patterns in non-equilibrium electrochemical deposition from oscillatory nucleation and growth," *Nature*, vol. 390, no. 6656, pp. 145–148, 1997.

[47] P. K. Yuen and V. N. Goral, "Low-cost rapid prototyping of flexible microfluidic devices using a desktop digital craft cutter," *Lab on a Chip*, vol. 10, no. 3, pp. 384–387, 2010.

[48] X. Yuan, L. Renaud, M.-C. Audry, and P. Kleimann, "Electrokinetic Biomolecule Preconcentration Using Xurography-Based Micro-Nano-Micro Fluidic Devices," *Analytical Chemistry*, vol. 87, no. 17, pp. 8695–8701, 2015.

[49] J. I. Martínez-López, M. Mojica, C. A. Rodríguez, and H. R. Siller, "Xurography as a Rapid Fabrication Alternative for Point-of-Care Devices: Assessment of Passive Micromixers," *Sensors*, vol. 16, no. 5, p. 705, 2016.

[50] A. Cesaratto, J. R. Lombardi, and M. Leona, "Tracking photo-degradation of triarylmethane dyes with surface-enhanced raman spectroscopy," *Journal of Raman Spectroscopy*, vol. 48, no. 3, pp. 418–424, 2017.

[51] L. Zhou, J. Zhou, W. Lai, X. Yang, J. Meng, L. Su, C. Gu, T. Jiang, E. Y. B. Pun, L. Shao, *et al.*, "Irreversible accumulated SERS behavior of the molecule-linked silver and silver-doped titanium dioxide hybrid system," *Nature Communications*, vol. 11, no. 1, p. 1785, 2020.

[52] T. T. Schaeffer, *Effects of light on materials in collections: data on photoflash and related sources*. Getty Publications, Los Angeles, 2001.

[53] S. Marimuthu, A. J. Antonisamy, S. Malayandi, K. Rajendran, P.-C. Tsai, A. Pugazhendhi, and V. K. Ponnusamy, "Silver nanoparticles in dye effluent treatment: A review on synthesis, treatment methods, mechanisms, photocatalytic degradation, toxic effects and mitigation of toxicity," *Journal of Photochemistry and Photobiology B: Biology*, vol. 205, p. 111823, 2020.

[54] D. Confortin, H. Neevel, M. Brustolon, L. Franco, A. J. Kettelarij, R. M. Williams, and M. R. van Bommel, "Crystal violet: study of the photo-fading of an early synthetic dye in aqueous solution and on paper with hplc-pda, lc-ms and fors," *Journal of Physics: Conference Series*, vol. 231, no. 1, p. 012011, 2010.

[55] H.-J. Butt, K. Graf, and M. Kappl, *Physics and chemistry of interfaces*. WILEY-VCH, Weinheim, Germany, 2013.

[56] M. K. Satapathy, P. Banerjee, and P. Das, "Plant-mediated synthesis of silver-nanocomposite as novel effective azo dye adsorbent," *Applied Nanoscience*, vol. 5, pp. 1–9, 2015.

[57] J.-B. Salmon and A. Ajdari, "Transverse transport of solutes between co-flowing pressure-driven streams for microfluidic studies of diffusion/reaction processes," *Journal of Applied Physics*, vol. 101, p. 074902, 04 2007.